

Temperature-insensitive long-wavelength ($\lambda \approx 14 \mu\text{m}$) Quantum Cascade lasers with low threshold

Xue Huang,* William O. Charles, and Claire Gmachl

Department of Electrical Engineering, Princeton University, Princeton, NJ 08544 USA

*xuehuang@princeton.edu

Abstract: We demonstrate high-performance, long-wavelength ($\lambda \approx 14 \mu\text{m}$) Quantum Cascade (QC) lasers based on a diagonal optical transition and a “two-phonon-continuum” depletion scheme in which the lower laser level is depopulated by resonant longitudinal optical phonon scattering followed by scattering to a lower energy level continuum. A 2.8 mm long QC laser shows a low threshold current density of 2.0 kA/cm^2 , a peak output power of $\sim 336 \text{ mW}$, and a slope efficiency of 375 mW/A , all at 300K , with a high characteristic temperature $T_0 \sim 310 \text{ K}$ over a wide temperature range from 240 K to 390 K .

©2011 Optical Society of America

OCIS codes: (140.3070) Infrared and far-infrared lasers; (230.5590) Quantum-well, -wire and -dot devices.

References and links

1. M. Troccoli, X. Wang, and J. Fan, “Quantum cascade lasers: high-power emission and single-mode operation in the long-wave infrared ($\lambda > 6 \mu\text{m}$),” *Opt. Eng.* **49**(11), 111106 (2010).
2. N. Bandyopadhyay, Y. Bai, B. Gokden, A. Myzaferi, S. Tsao, S. Slivken, and M. Razeghi, “Watt level performance of quantum cascade lasers in room temperature continuous wave operation at $\lambda \sim 3.76 \mu\text{m}$,” *Appl. Phys. Lett.* **97**(13), 131117 (2010).
3. S. Slivken, A. Evans, W. Zhang, and M. Razeghi, “High-power, continuous-operation intersubband laser for wavelengths greater than $10 \mu\text{m}$,” *Appl. Phys. Lett.* **90**(15), 151115 (2007).
4. R. F. Curl, F. Capasso, C. F. Gmachl, A. A. Kosterev, B. McManus, R. Lewicki, M. Pusharsky, G. Wysocki, and F. K. Tittel, “Quantum cascade lasers in chemical physics,” *Chem. Phys. Lett.* **487**(1-3), 1–18 (2010).
5. I. Sydoryk, A. Lim, W. Jäger, J. Tulip, and M. T. Parsons, “Detection of benzene and toluene gases using a midinfrared continuous-wave external cavity quantum cascade laser at atmospheric pressure,” *Appl. Opt.* **49**(6), 945–949 (2010).
6. R. Lewicki, A. A. Kosterev, F. Toor, Y. Yao, C. F. Gmachl, T. Tsai, G. Wysocki, X. Wang, M. Troccoli, M. Fong, and F. K. Tittel, “Quantum cascade laser absorption spectroscopy of UF_6 at $7.74 \mu\text{m}$ for analytical uranium enrichment measurements,” *Proc. SPIE* **7608**, 76080E (2002).
7. A. Tredicucci, C. Gmachl, F. Capasso, D. L. Sivco, A. L. Hutchinson, and A. Y. Cho, “Long wavelength superlattice quantum cascade lasers at $\lambda = 17 \mu\text{m}$,” *Appl. Phys. Lett.* **74**(5), 638–640 (1999).
8. M. Rochat, D. Hofstetter, M. Beck, and J. Faist, “Long-wavelength ($\lambda \approx 16 \mu\text{m}$), room-temperature, single-frequency quantum-cascade lasers based on a bound-to-continuum transition,” *Appl. Phys. Lett.* **79**(26), 4271–4273 (2001).
9. K. Fujita, M. Yamanishi, T. Edamura, A. Sugiyama, and S. Furuta, “Extremely high T_0 -values ($\sim 450 \text{ K}$) of long-wavelength ($\sim 15 \mu\text{m}$), low-threshold-current-density quantum-cascade lasers based on the indirect pump scheme,” *Appl. Phys. Lett.* **97**, 201109 (2010).
10. J. Faist, F. Capasso, D. L. Sivco, C. Sirtori, A. L. Hutchinson, and A. Y. Cho, “Quantum cascade laser,” *Science* **264**(5158), 553–556 (1994).
11. A. Bismuto, R. Terazzi, M. Beck, and J. Faist, “Electrically tunable, high performance quantum cascade laser,” *Appl. Phys. Lett.* **96**(14), 141105 (2010).
12. D. Hofstetter, M. Beck, T. Aellen, and J. Faist, “High-temperature operation of distributed feedback quantum-cascade lasers at $5.3 \mu\text{m}$,” *Appl. Phys. Lett.* **78**(4), 396–398 (2001).
13. J. Faist, M. Beck, T. Aellen, and E. Gini, “Quantum-cascade lasers based on a bound-to-continuum transition,” *Appl. Phys. Lett.* **78**(2), 147–149 (2001).
14. K. Fujita, S. Furuta, A. Sugiyama, T. Ochiai, T. Edamura, N. Akikusa, M. Yamanishi, and H. Kan, “Room temperature, continuous-wave operation of quantum cascade lasers with single phonon resonance-continuum depopulation structures grown by metal organic vapor-phase epitaxy,” *Appl. Phys. Lett.* **91**(14), 141121 (2007).

15. M. Escarra, A. J. Hoffman, K. J. Franz, S. S. Howard, R. Cendejas, X. Wang, J. Y. Fan, and C. F. Gmachl, "Quantum cascade lasers with voltage defect of less than one longitudinal optical phonon energy," *Appl. Phys. Lett.* **94**(25), 251114 (2009).
16. A. Lops, V. Spagnolo, and G. Scamarcio, "Thermal modeling of GaInAs/AlInAs quantum cascade lasers," *J. Appl. Phys.* **100**(4), 043109 (2006).

1. Introduction

Recent improvements in Quantum-Cascade (QC) lasers have lead to room-temperature continuous-wave (CW) operation with high power (> 100 mW) output in the 3.8-10.6 μm range [1–3]. With availability of high performance in this wavelength range, QC lasers have successfully been applied in various trace gas sensing applications [4]. However, lack of high performance for longer wavelengths in the 12 ~16 μm range, where the strongest absorption lines of e.g. BTEX (benzene, toluene, ethylbenzene, and xylenes) or uranium hexafluoride are, so far hinders QC laser applications in sensing of these important gases. One alternative are the much weaker absorption lines in the 3.8-10.6 μm range. For example, an external-cavity (EC) CW QC laser was used to detect benzene gas with ν_{14} band absorption at ~ 10 μm , with an experimental detection limit of 0.26 ppm [5]. The line strength of the ν_{14} band near 10 μm is about one order of magnitude weaker than that of the ν_4 band at ~ 14.8 μm . Another example is an EC QC laser targeting the $\nu_1 + \nu_3$ combination band of uranium hexafluoride (UF_6) at 7.74 μm [6]. However, the absorption from the ν_3 band at ~ 16 μm is about 500 times that of the $\nu_1 + \nu_3$ combination band. Evidently, improvement on the detection sensitivity of QC-laser based sensing for these gases requires high-performance QC lasers in the 12 ~16 μm range.

Compared with short-wavelength QC lasers, there are four main challenges for long-wavelength QC lasers. First, a large population inversion is more difficult to attain, since the lifetime of the upper laser level drops as the optical transition energy decreases due to a higher longitudinal optical (LO) photon scattering rate. Second, the leakage from the injector directly to the lower laser level is similarly high. Third, the small photon energy leads to low voltage efficiency, the ratio of the photon energy drop to the total energy drop across the whole structure. Finally, the waveguide loss due to free-carrier absorption is roughly proportional to the square of the wavelength of light [7]. All the above challenges lead to high threshold current density and low output power for long-wavelength QC lasers [7–9]. The best report so far with a wavelength in the 14 - 15.5 μm range demonstrated a room temperature threshold current density of 3.5 kA/cm^2 from a 4 mm long laser with HR-coated back facet [9].

In this work, we demonstrate a high-performance long-wavelength QC laser emitting at ~ 14 μm , optimized by employing a diagonal optical transition and a "two-phonon-continuum" depletion scheme, in which the lower laser level is depleted by resonant one LO-phonon scattering to the level below it, followed by scattering to a lower level continuum about two LO-phonon below the lower laser level. A 2.8 mm long, 38 μm wide QC laser with HR-coated back facet shows a low threshold current density of 2.0 kA/cm^2 , which is a clear improvement over earlier reports, an output power of 336 mW, and a slope efficiency of 375 mW/A at 300 K, as well as a high characteristic temperature ~ 310 K over a wide temperature range around room temperature (240-390 K).

2. Quantum cascade structure design and laser fabrication

A portion of the conduction band of this ~ 14 μm (~ 89 meV) QC laser structure is depicted in Fig. 1 at an applied electric field of 35 kV/cm . The layer sequence of a single stage is (in Angstroms, electron-downstream starting from the injection barrier) **37/29/8/55/6/56/7/52/8/47/14/45/19/44/21/40/26/37/27/35/28/32**, where $\text{In}_{0.52}\text{Al}_{0.48}\text{As}$ barriers are in bold and $\text{In}_{0.53}\text{Ga}_{0.47}\text{As}$ wells are in normal font. Underlined layers are Si-doped to $n = 1.5 \times 10^{17} \text{ cm}^{-3}$. By employing a diagonal optical transition [10, 11], the overlap between the upper laser level and lower levels is reduced in order to obtain a long lifetime (> 2.0 ps) for the upper laser level. Also, the non-localized upper laser level penetrates deep to the injector region, hence enabling electron injection by both resonant tunneling from the injector ground level and

phonon-assisted scattering directly from higher injector levels. Moreover, the depopulation of the lower laser level is achieved by a “two-phonon-continuum” scheme, with the lower laser level depleted by one LO-phonon scattering to a single level “II” below it, followed by scattering from level “II” to the lower energy level continuum through LO-phonon scattering again. The advantages of the two-phonon resonance design (optical transition into an isolated lower lasing level) [12] and bound-to-continuum design (fast electron extraction through miniband from the active region to the injector) [13] are combined in this approach. This “two-phonon-continuum” scheme is in contrast with the existing single phonon resonance-continuum depopulation (SPC) scheme of [14], with which it shares the characteristics of at least one LO-phonon resonance to a level continuum. However, in the SPC design, the exit barrier is designed carefully to suppress the extension of wavefunctions from the injector miniband to the active region, in order to obtain a bound-to-bound optical transition [14]. By contrast, in the “two-phonon-continuum” scheme reported here the entire injector miniband was designed to penetrate deeply into the active region and below level “II” (see Fig. 1), in order to form a wide continuum of ~ 70 meV, which leads to efficient electron extraction to the injector and fast transport to the upper laser level in the following active region. At the same time, the bound-to-bound lasing transition is still guaranteed, since the continuum is well below the lower lasing level and level “II”. In order to prevent thermal backfilling of electrons to the lower laser level, the separation between the lower laser level and ground level of the next injector is designed to be large (~ 150 meV). Furthermore, the next upper level in the active region is ~ 63 meV above the upper laser level, to suppress electron leakage via the upper laser level assisted by phonon absorption and scattering to the states above.

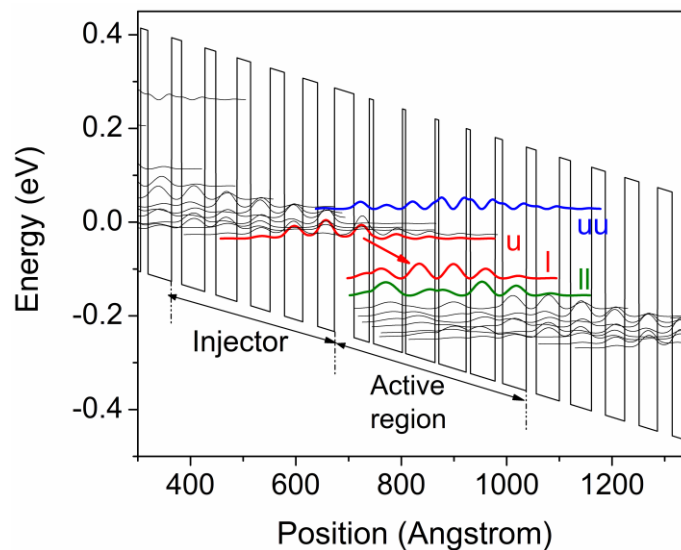


Fig. 1. A portion of the conduction band diagram of the $\lambda \sim 14$ μm QC laser structure with the moduli squared of the relevant wave functions at an electric field of 35 kV/cm at 300 K. The optical transition is indicated by the red arrow. The red indicated levels “u” and “l” are the upper and lower laser levels, respectively. The “two-phonon-continuum” depletion is achieved through the green marked level “II” and the level continuum below it. The blue marked level “uu” is ~ 63 meV above the upper laser level.

This QC structure was grown by solid source molecular beam epitaxy (MBE), with $\text{In}_{0.52}\text{Al}_{0.48}\text{As}$ and $\text{In}_{0.53}\text{Ga}_{0.47}\text{As}$ lattice matched to a low doped ($n \sim 1.4 \times 10^{17} \text{ cm}^{-3}$) InP substrate. The active core includes 70 stages of repeated alternating active and injector regions, which are sandwiched between a $0.4 \mu\text{m}$ thick $\text{In}_{0.53}\text{Ga}_{0.47}\text{As}$ lower waveguide layer (doped $n \sim 5 \times 10^{16} \text{ cm}^{-3}$) and a $0.2 \mu\text{m}$ thick $\text{In}_{0.53}\text{Ga}_{0.47}\text{As}$ upper waveguide layer (doped $n \sim 5 \times 10^{16} \text{ cm}^{-3}$). The upper cladding consists of a $2.4 \mu\text{m}$ thick $\text{In}_{0.52}\text{Al}_{0.48}\text{As}$ layer (doped

$n \sim 5 \times 10^{16} \text{ cm}^{-3}$), followed by a 0.6 μm thick $\text{In}_{0.53}\text{Ga}_{0.47}\text{As}$ plasmon layer (doped $n \sim 5 \times 10^{18} \text{ cm}^{-3}$) and a 0.05 μm thick $\text{In}_{0.53}\text{Ga}_{0.47}\text{As}$ contact layer (doped $n \sim 2 \times 10^{19} \text{ cm}^{-3}$). Deep-etched ridge waveguide lasers were processed with ridge widths from 25 μm to 40 μm and cavity lengths from 1.9 mm to 3.8 mm.

3. Characterization and temperature-insensitive, low-threshold performance

Laser spectra at different temperatures and at 1.1 times threshold current densities are shown in Fig. 2. The emission wavelengths are around $\sim 14 \mu\text{m}$. The light-current-voltage (LIV) characteristics of a 2.8 mm long, 38 μm wide QC laser with HR-coating for the back facet in pulsed mode are shown in Fig. 3, where the power is collected by a nitrogen-cooled HgCdTe detector. The threshold current densities at 80 K and 300 K are 0.76 kA/cm^2 and 2.0 kA/cm^2 , respectively. At 80 K, the peak output power is 1.4 W and the slope efficiency is 513 mW/A . At 300 K, the peak power is 336 mW , with a slope efficiency of 375 mW/A .

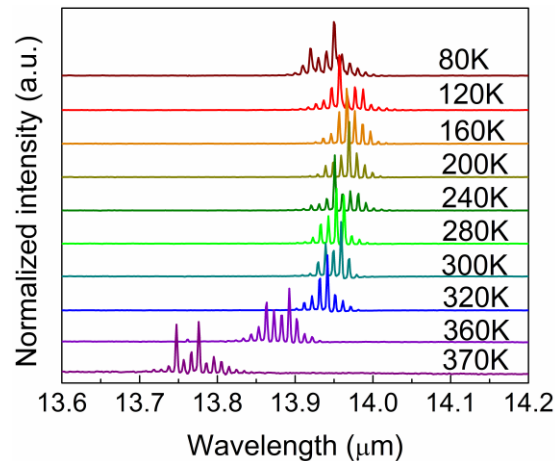


Fig. 2. Laser spectra of a 3.8 mm long, 38 μm wide QC laser with an applied current density of 1.1 times the threshold density, from 80 K to 370 K.

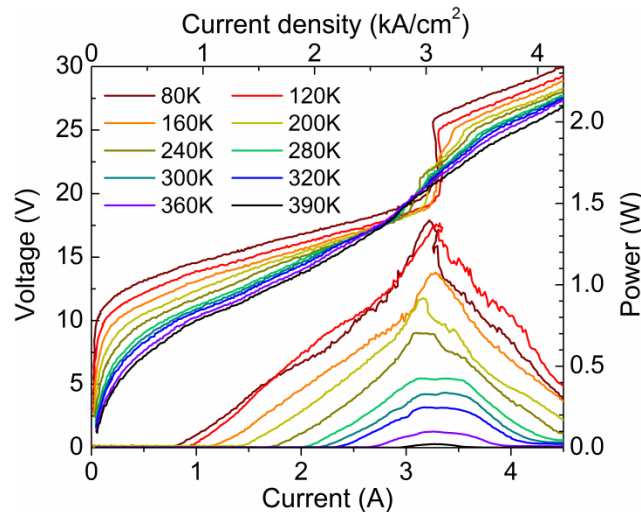


Fig. 3. Pulsed LIV characteristics for a 2.8 mm long, 38 μm wide HR- back facet coated QC laser at the indicated heat-sink temperatures, from 80 K to 390 K. The pulse width is 100 ns, and the repetition rate is 4 kHz.

Due to optimization of the design to attain efficient electron injection and extraction, and to reduce thermal backfilling and carrier leakage as described above, good high-temperature performance is demonstrated with a high characteristic temperature T_0 of the threshold current density. Fit by the empirical exponential function $J_{th}(T) = J_0 \exp(T/T_0)$, $T_0 = 189\text{ K}$ in the 80 K – 240 K range and $T_0 = 306\text{ K}$ in the 240– 390 K range are obtained for the specific laser of Fig. 3 (see Fig. 4(a)). The improvement in T_0 in the higher temperature range can be explained by the change of energy difference E_{l-d} between the lower laser level and the level directly below it at threshold with temperature (see Fig. 4(a)). From the calculated conduction band diagram at the electric field corresponding to the measured threshold voltage (see Fig. 3), E_{l-d} is smaller than the energy of a LO-phonon below 240K, but it becomes equal or larger than the energy of a LO-phonon above 240 K, leading to a higher depletion rate of the lower laser level by one LO-phonon scattering, therefore the LO-phonon scattering lifetime of the lower laser level changes from $\sim 0.4\text{ ps}$ below 240 K to $\leq 0.2\text{ ps}$ above 240 K. This improvement in depletion of the lower laser level partly compensates thermal backfilling and slows down the increase of threshold with temperature above 240 K. Similar discontinuity in temperature performance was observed in a QC laser with a total voltage defect per stage of less than one LO-phonon energy [15].

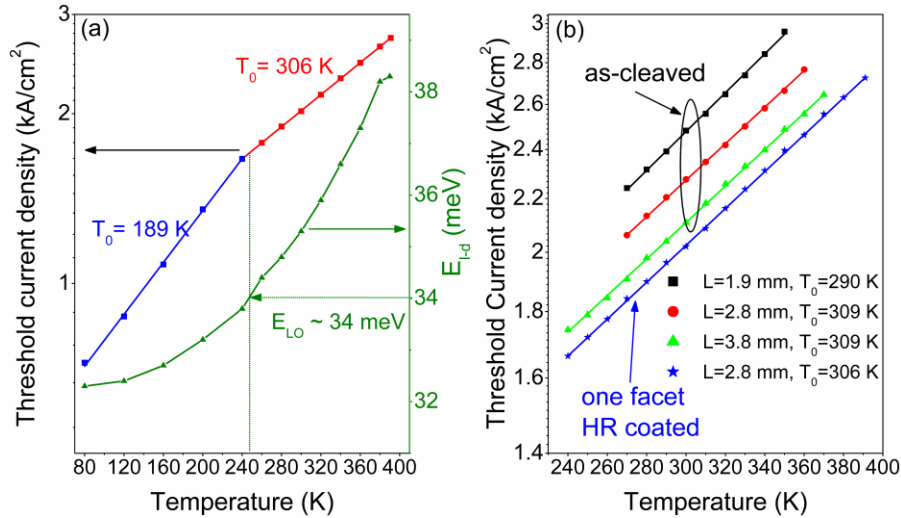


Fig. 4. (a) Threshold current density (blue and red squares) and energy difference E_{l-d} between the lower laser level and the level directly below it (green triangles) vs. heat-sink temperature, for the 2.8 mm long, 38 μm wide QC laser. The blue and red solid lines are exponential fits to the data, showing two different regions with different characteristic temperatures, $T_0 = 189\text{ K}$ from 80 K to 240 K and $T_0 = 306\text{ K}$ from 240 K to 390 K. Improvement of T_0 occurs where E_{l-d} at threshold becomes larger than one LO-phonon, as shown by the dashed green arrow. (b) Threshold current density of 38 μm wide QC lasers with different cavity lengths (1.9 mm, 2.8 mm, and 3.8 mm). Three lasers are with two as-cleaved facets, and one 2.8 mm long laser has a HR-coating on the back facet. The solid curves are exponential fits to the data, from which different characteristic temperatures around room temperature are extracted.

The threshold current densities of lasers with different cavity lengths from 1.9 mm to 3.8 mm are plotted and exponentially fit in Fig. 4(b) around room temperature, all with a characteristic temperature $T_0 \sim 300\text{ K}$. The highest characteristic temperature $T_0 = 309\text{ K}$ was achieved with both the 2.8 mm long and 3.8 mm long lasers without HR coating.

The average power under high duty cycle (5% ~30%) operation from 80 K to 300 K is also measured by a thermopile detector (see Fig. 5), from the 2.8 mm long laser. A maximum average power $\sim 130\text{ mW}$ is achieved with a duty cycle of 20% (1 μs pulses at 200 kHz) at 80 K, while at 300 K an average power of $\sim 6\text{ mW}$ is obtained with a duty cycle of 5% (0.5 μs pulses at 100 kHz).

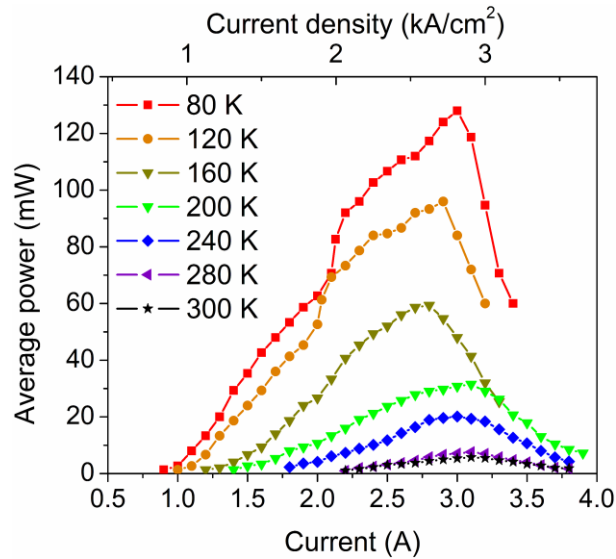


Fig. 5. Light-current characteristics of a 2.8 mm long, 38 μm wide laser, with average power measured by a thermopile detector, from 80 K to 300 K. The duty cycle optimized for maximum average power is 20% (pulse width 1 μs , repetition rate 200 kHz) from 80 K to 160 K, 7.5% (pulse width 0.5 μs , repetition rate 150 kHz) from 200 K to 240 K, and 5% (pulse width 0.5 μs , repetition rate 100 kHz) from 280 K to 300 K.

4. Discussion on voltage efficiency, power consumption and summary

The voltage efficiency at threshold at 300 K is 41% (see Fig. 3), i.e. the ratio of the photon energy to the total voltage drop per stage, which is low compared to shorter-wavelength QC lasers [15]. Voltage efficiency can be improved by decreasing the separation between the lower laser level and ground level of the next injector. However it means sacrificing the high-temperature performance due to thermal backfilling at the same time. More effort is still needed to improve the voltage efficiency of long-wavelength QC lasers, without deteriorating the high-temperature performance.

The $\text{In}_{0.52}\text{Al}_{0.48}\text{As}$ cladding layers (doped $n \sim 5 \times 10^{16} \text{ cm}^{-3}$) used in this QC structure have a comparatively low thermal conductivity [16]. And the large number (70) of cascaded stages leads to a high voltage ($\sim 15 \text{ V}$ at 300 K) at threshold. Therefore the high input power density (30 kW/cm^2) is still a challenge for thermal dissipation in pursuit of CW operation. However, further improvement can be expected if InP layers are adopted as the lower and upper cladding to improve thermal dissipation, combined with low doping ($n \sim 2 \times 10^{16} \text{ cm}^{-3}$) to reduce free-carrier absorption. From mode simulation, the same threshold current density can be achieved if 50 stages are sandwiched between a 1.8 μm thick lower InP cladding and a 3.4 μm thick upper InP cladding (both doped $n \sim 2 \times 10^{16} \text{ cm}^{-3}$), leading to an expected power consumption of only 21 kW/cm^2 .

In conclusion, we demonstrate a long-wavelength QC laser design at $\sim 14 \mu\text{m}$ wavelength, which is optimized to attain efficient electron injection and extraction, and to reduce thermal backfilling and carrier activation leakage. A 2.8 mm long, 38 μm wide QC laser with HR-coated back facet has a low threshold current density of 2.0 kA/cm^2 , an output power of 336 mW, and a slope efficiency of 375 mW/A, all at 300 K, as well as a high characteristic temperature $T_0 \sim 310 \text{ K}$ in a wide range from 240 K to 390 K.

Acknowledgements

This work is supported in part by MIRTHE (NSF-ERC).